Journal of Materials Chemistry A

Highly Stable Ordered Intermetallic PtCo Alloy Catalyst Supported on Graphitized Carbon Containing Co@CN for Oxygen Reduction Reaction

Journal:	*Journal of Materials Chemistry A*
Manuscript ID	TA-ART-05-2020-005182.R2
Article Type:	Paper
Date Submitted by the Author:	06-Aug-2020
Complete List of Authors:	Jung , Won Suk; Hankyong National University, Department of Chemical Engineering Lee, Woong Hee; Korea Institute of Science and Technology, Clean Energy Research Center, Oh, Hyung-Suk; Korea Institute of Science and Technology, Clean Energy Research Center Popov, Branko; University of South Carolina, Department of Chemical Engineering

PAPER

Highly Stable Ordered Intermetallic PtCo Alloy Catalyst Supported on Graphitized Carbon Containing Co@CN for Oxygen Reduction Reaction

Received 00th January 20xx,
Accepted 00th January 20xx

DOI: 10.1039/x0xx00000x

Won Suk Jung [a]*, Woong Hee Lee [b], Hyung-Suk Oh [b, c, d]*, and Branko N. Popov [e]*

PtCo alloy catalyst is prepared by thermal diffusion of Co encapsulated with thin N-doped carbon layers on graphitic carbon into Pt lattice (PtCo/NGC). Co diffuses up to the near-Pt surface, which results in the intermetallic PtCo structure without the leaching process. The intermetallic PtCo structure thermally treated under optimized conditions shows 3-fold higher mass activity than the commercial Pt/C. Potential and maximum power density loss of PtCo/NGC after 30,000 potential cycles are 34 mV and 11%, respectively, which indicates that the PtCo/NGC is remarkably stable when compared to commercial Pt/C and commercial PtCo/GC catalysts. The enhanced catalytic performance and stability of the PtCo/NGC catalyst are attributed to the formation of an intermetallic structure that alleviates the Pt oxidation and Co dissolution. The outstanding performance and stability qualify the ordered intermetallic PtCo/NGC to be a promising cathode catalyst for the commercialization of fuel cells.

1. Introduction

Proton exchange membrane fuel cells (PEMFCs) enable the direct production of electricity from chemicals with high efficiency, noiseless operation, and without pollutant emissions as compared to conventional internal combustions engines. However, the sluggish kinetics of oxygen reduction reaction (ORR), cost, and durability of catalyst inhibit the use of PEMFC's to advance to commercialization. In general, the catalysts are comprised of Pt-based nanoparticles and high surface area carbon which has the ideal properties as a support such as high electrical conductivity, surface area, and porosity. Degradation mechanisms for PEMFCs involve the Pt-based catalysts and carbon-based supports. In particular, Pt-based catalysts are suffering from the dissolution of Pt [1-3], migration of Pt [4, 5], and Pt agglomeration [6, 7] in acidic and high potential conditions.

A limited supply of Pt, the high cost with its sluggish kinetics for oxygen reduction reaction (ORR) triggered the research and development of various Pt-alloy cathode catalysts.[8-21] Wu et al. presented a one-pot synthesis of Pt-Pd bimetallic catalyst with nanodendritic structures for the ORR.[22] Different ratios of Pt and Pd were prepared and studied by structural and electrochemical characterizations. The Pt_1Pd_1/C catalyst showed an enhanced mass activity of 1.164 A mg_{Pt}^{-1} and specific activity of 1.33 mA cm^{-2}, as compared to those of commercial Pt/C catalysts (0.15 A mg_{Pt}^{-1} for mass activity, and 0.25 mA cm^{-2} for a specific activity). The durability test indicated that the catalyst exhibited remarkably stable performance after 10,000 cycles. 10 nm-sized octahedral PtCu alloy catalysts were synthesized using I^- as shape-directing agent.[20] They found that the stability of PtCu/C could be improved by doping trace Au, which resulted from the suppression of diffusion/dissolution of low-coordinated Pt atoms. Li et al. prepared carbon-supported 1 nm-thick PtNiRh trimetallic nanowires catalyst via a surfactant-assisted synthetic route. The role of alloyed Rh atoms in improving the catalytic durability of Pt-based catalyst was also supported by DFT calculations. Since vacancy formation energies of outmost Pt and Ni atoms represent the tendency of dissolution of Pt atoms and leaching of Ni atoms, respectively, the effects of Rh atoms on vacancy formation energies of Pt and Ni atoms were investigated for the catalysts. The enhancement in measured activity over Pt by alloying Pt with transition metals can be explained by various factors including lowering of the Pt oxidation state[23], suppression of Pt oxide formation[23, 24], formation of a new electronic structure with higher Pt 5d orbital vacancies[25], decrease in the Pt-Pt interatomic distance and therefore a more favorable O_2 adsorption[25], formation of a thin Pt skin on the surface of the alloy core[26-28], and the altered electronic structures of the topmost Pt atoms.[29-31]

[a] Department of Chemical Engineering, Hankyong National University, Jungang-ro 327, Anseong-si, Gyeonggi-do, 17579, Republic of Korea
[b] Clean Energy Research Center, Korea Institute of Science and Technology (KIST), Hwarang-ro 14-gil 5, Seongbuk-gu, Seoul, 02792, Republic of Korea
[c] Division of Energy and Environmental Technology, KIST school, Korea University of Science and Technology, Seoul 02792, Republic of Korea.
[d] KHU-KIST Department of Conversing Science and Technology, Kyung Hee University, Seoul 02447, Republic of Korea.
[e] Center for Electrochemical Engineering, Department of Chemical Engineering, University of South Carolina, Columbia, SC, 29208, USA
*Corresponding author
Email: jungw@khnu.ac.kr, hyung-suk.oh@kist.re.kr, popov@cec.sc.edu

Electronic Supplementary Information (ESI) available: [details of any supplementary information available should be included here. See DOI: 10.1039/x0xx00000x

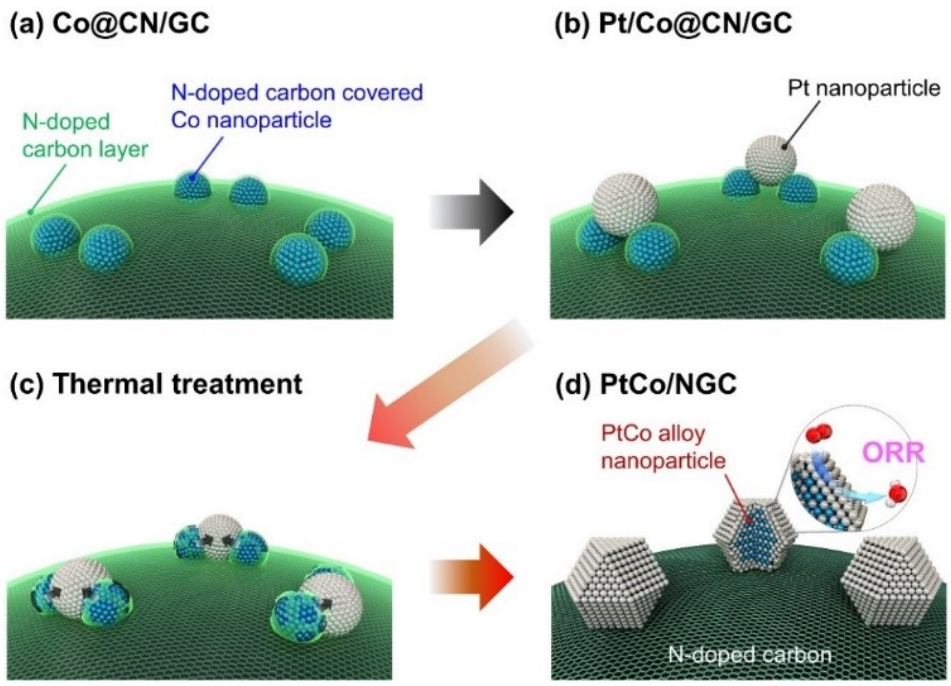

Scheme 1. Schematic illustration of the synthetic process of the ordered intermetallic PtCo/NGC for ORR: (a) Co encapsulated with CN layers on GC (Co@CN/GC); (b) Pt nanoparticles deposited on Co@CN/GC by modified polyol method; (c) Co diffused to the Pt lattice to form the ordered intermetallic alloy; and (d) the formation of ordered intermetallic PtCo on NGC.

Carpenter et al. used of N,N-dimethylformamide (DMF) as both solvent and reductant in the solvothermal synthesis of PtNi catalysts.[8] Well-faceted Pt_3Ni alloy nanocrystals exhibited ca. 15 times higher activity than commercial Pt/C catalyst and stable up to 20,000 cycles in a rotating disk electrode (RDE) set-up. Wang et al. showed PtCo catalysts composed of ordered Pt_3Co intermetallic cores with a 2 – 3 atomic-layer-thick platinum shell.[32] Mass activity and specific activity of ordered Pt_3Co alloy catalysts increased over 2-fold and 3-fold higher than those of the disordered Pt_3Co alloy catalysts, while the ordered Pt_3Co alloy catalysts were stable after 5,000 cycles. Stassi et al. investigated the effect of thermal treatment on the structure and surface composition of PtCo catalysts during the accelerated stress test (AST).[33] They reported that different thermal treatments caused significant structural and morphological modifications in the PtCo catalysts. Yu et al. studied the cycling stability of dealloyed $PtCo_3$ and $PtCu_3$ catalysts between 0.6 and 1.0 V (vs. RHE) for up to 30,000 cycles.[34] *In-situ/operando* X-ray absorption spectroscopy (XAS) analysis showed stronger bulk Pt-Pt compressive strains and higher bulk *d*-band vacancies for the dealloyed $PtCu_3$ than the dealloyed $PtCo_3$ which was correlated to the higher initial activity of dealloyed $PtCu_3$. However, membrane electrode assembly (MEA) tests showed poor durability towards voltage cycling for the dealloyed $PtCu_3$ catalyst when compared to dealloyed $PtCo_3$ catalyst due to Cu plating on the anode.

There is a concern for the carbon corrosion due to presence of high water content, high oxygen concentration, low pH, high temperature (70 – 80 ℃) and very high potentials (1.2 – 1.5 V vs. RHE) at the cathode interface during start-up/shut down cycles and fuel starvation. The carbon can be oxidized to CO_2 at 0.207 V at room temperature. Han et al. reported that the potential loss at high current densities was significantly decreased by shifting the upper potential from 1.0 V to 0.925 V.[35]

The previous research indicated that clearly there is a need to develop both the advanced catalyst and support for the successful commercialization of PEMFCs. In this study, we developed an ordered intermetallic face-centered tetragonal (fct) Pt-based alloy catalyst with high activity and stability. Initially, Co and N were introduced into the graphitized carbon (GC) support by pyrolyzing a mixture of Co and N precursors. Co protected with the N-doped graphitic carbon shells was later used for the formation of PtCo catalyst. Thus prepared support is denoted as Co@CN on GC (Co@CN/GC). After the Pt deposition by modified polyol method (Pt/Co@CN/GC), the controlled heat-treatment was applied to form PtCo/NGC under a reducing atmosphere. At this step, the Co, which was previously incorporated within the N-doped graphitic carbon shells, diffuses up to the surface and forms PtCo/NGC alloy catalyst. A single cell test was carried out to evaluate the performance and durability of the catalyst. The durability of the catalyst was studied by potential cycling between 0.6 – 1.0 V for 30,000 cycles. Next, the activity and durability of PtCo/NGC catalyst were examined and compared with those of commercial PtCo/GC as well as with the state-of-the-art Pt/C catalysts.

2. Experimental Section

2.1. Preparation of support and catalyst.

To obtain Co@CN/GC, as-received CB (Ketjen Black EC-300J) was heat-treated at 1700 ℃ for 2 h under N_2 atmosphere, which is denoted as GC (Figure S1). Then, the material was oxidized in 9.8 M HNO_3 solution at 85 ℃ for 9 h under reflux.

After filtering, the oxidized carbon was washed with de-ionized (DI) water several times and dried under vacuum at 80 ℃ for 12 h. The desired amount of $Co(NO_3)_2$ and ethylenediamine, used as Co and N precursors, respectively, were mixed with the oxidized carbon in 200 ml isopropyl alcohol (IPA, BDH Chemicals). The mol ratio of Co and N precursors was maintained at 1:9. The mixture was refluxed for 3 h at 85 ℃ under vigorous stirring, followed by drying under vacuum at 80 ℃. The resultant powder was subjected to heat-treatment under inert atmosphere at 800 ℃ for 1 h followed by leaching in 0.5 M H_2SO_4 at 80 ℃ for 3 h to remove excess Co. The final product is denoted as Co@CN/GC. The supports were non-covalently activated by the pyrenecarboxylic acid before the Pt deposition due to their high hydrophobicity deposition. [36]

Pt deposition was accomplished by a polyol reduction method for the preparation of 30% Pt/Co@CN/GC catalyst. First, the Co@CN/GC was dispersed in 25 ml of ethylene glycol in a sonication bath. A desired amount of $PtCl_4$ was added and the pH was adjusted to 11 by the addition of 0.5 M NaOH solution. The resulting solution was refluxed at 160 ℃ for 3 h and allowed to cool to room temperature. Then, the solution was filtered, washed with DI water, and dried at 160 ℃ for 1 h. Prior to heat-treatment, the Pt/Co@CN/GC was subjected to a protective coating procedure. Oxidative polymerization of aniline sulfate was carried out at room temperature using ammonium peroxysulfate as the oxidizing agent.[37] The polyaniline-coated Pt/Co@CN/GC was placed in an alumina crucible and heat-treated at 800 ℃ or 2 h in a tubular furnace under 5% H_2 (balance N_2) atmosphere. The catalyst thus prepared is denoted as PtCo/NGC.

2.2. Physical characterization.

The nitrogen adsorption/desorption isotherms were obtained at −196 ℃ using a Quantachrome NOVA 2000 BET analyzer. The specific surface area was determined by a multipoint BET analysis. PSD curves were calculated by the BJH method using the adsorption/desorption branch. XRD analysis was performed using a Rigaku D/Max 2500 V/ PC with a Cu Kα radiation. A tube voltage of 30 kV and a current of 15 mA were used during the scanning. Raman spectroscopy was used to evaluate the degree of graphitization of the carbon supports using HORIBA "LABRAM 1B" (He-Ne 20 mW laser, wavelength 632.817 nm). ICP-AES (Perkin Elmer) analysis was used to determine the composition of the catalysts. HR-TEM was used to study the morphology and particle size distribution of the catalysts using Hitachi 9500 HRTEM operated at 300 kV accelerating voltage. XRF (Fischer XDAL) was used to determine PtCo composition in the catalyst and Pt loading in the catalyst coated membrane.

2.3 MEA fabrication and electrochemical measurement.

The PtCo/NGC catalyst was employed as the cathode catalyst while commercial Pt/C (TEC10E50E, Tanaka Kikinzoku Kogyo K.K.) was used as a catalyst for the anode. Catalyst inks were prepared by ultrasonically mixing the appropriate amount of catalysts, IPA, Nafion® ionomer (5% solution, Alfa Aesar), and DI water. The ionomer content was 30% and 20% in the anode and cathode inks, respectively. The catalyst inks were sprayed directly on the Nafion® 212 membrane covering an active area of 25 cm^2. The Pt loading on the anode and cathode electrodes is kept at 0.1 and 0.1 mg cm^{-2}, respectively. The catalyst coated membrane was then hot pressed at 140 ℃ using a pressure of 20 kg cm^{-2} for 6 min. in between the gas diffusion layers (Sigracet GDL 10BC, SGL) and Teflon gaskets to prepare the MEA for the performance evaluation studies in fuel cells.

The fuel cell polarization was conducted using a fully automated fuel cell test station (Scribner Associates Inc., model 850e) at 80 ℃. H_2 and air were supplied to the anode and cathode at the constant stoichiometry of 2 and 2 applying the backpressure of 170 kPa_{abs}. The measurement was carried out at 60% relative humidity (RH). The mass activity at 0.9 $V_{iR\text{-}free}$ was evaluated under H_2/O_2 (2/9.5 stoic.) at 80 ℃, 100% RH, and 150 $kPa_{abs.}$ back pressure. The ECSA was estimated using cyclic voltammetry (CV) experiments carried out between 0.05 and 0.6 V (vs. RHE) at 80 ℃ under fully humidified H_2 and N_2 supply to the anode and the cathode, respectively. The ECSA measurements were performed after 0, 100, 1000, 5000, 10,000, and 30,000 cycles. In AST, 200 sccm H_2 and 75 sccm N_2 were supplied to the anode and cathode, respectively and the potential was swept between 0.6 and 1.0 V (vs. RHE) at 50 mV s^{-1} in a triangle profile for up to 30,000 cycles, since it has been estimated that the cathode catalysts undergo 30,000 potential cycles under operating conditions. For comparison purposes, MEAs with commercial PtCo/GC (TEC36EA52, Tanaka Kikinzoku Kogyo K.K.) and Pt/C as cathode catalysts were also prepared and evaluated under the same experimental conditions.

3. Results and Discussion

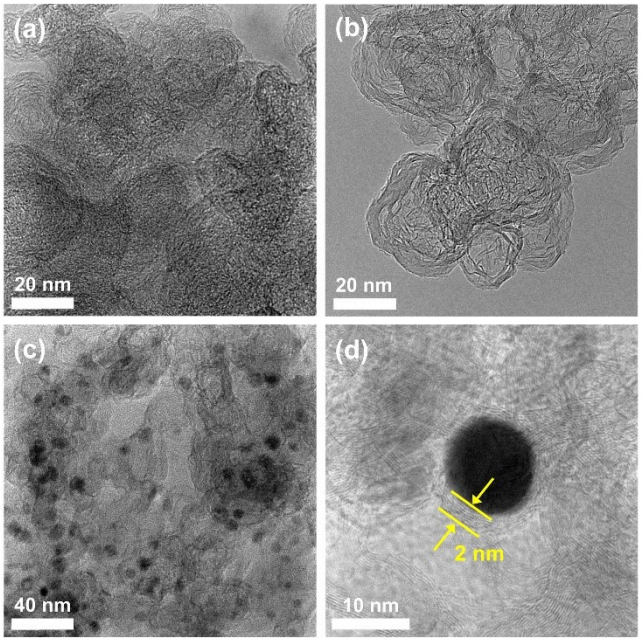

Figure 1. HR-TEM images of (a) carbon black (denoted to CB), (b) graphitized carbon black by heat treatment (denoted to GC), (c) Co@CN/GC and (d) graphitic carbon shell thickness of Co@CN/GC.

The morphology of CB, GC, and Co@CN/GC supports was studied using a high-resolution transmission electron microscope (HR-TEM) technique The HR-TEM images of CB, GC and Co@CN/GC are shown in Figure 1a-c. The GC and Co@CN/GC show the apparent graphitic carbon layer as compared to the amorphous CB with discontinuous graphite sheets. The hollow morphology is observed and sealed off by graphitic layers being seen as the thick dark fringes in GC. The apparent difference between GC and Co@CN/GC is the presence of Co particles protected with graphitized CN shells (2 nm thickness) as shown in Figure 1d. The unstable Co particles on the surface are removed during acid leaching. Nanostructured fibers or tubes of graphitic carbon are also formed as a result of pyrolysis in the presence of Co metal.[38, 39] Inductively coupled plasma atomic emission spectroscopy (ICP-AES) results of Co@CN/GC indicated a cobalt content of ca. 13 wt% in the supports synthesized at 800 ℃.

Figure 2a and 2b show the nitrogen adsorption-desorption isotherms and Barrett–Joyner–Halenda (BJH) pore size distribution (PSD) curves of CB and Co@CN/GC, which determines the porous characteristics and the pore size. The specific surface area of CB is 826.4 m^2 g^{-1}, while the Co@CN/GC has 284.3 m^2 g^{-1}. The isotherm of Co@CN/GC shows a hysteresis loop with sharp adsorption and desorption branches over a relative pressure range of 0.4-0.8. In addition, nitrogen uptake for the Co@CN/GC is observed at a relatively high pressure of 0.94-1.0, which is associated with the presence of mesopores.[40] The isotherm of Co@CN/GC exhibits characteristic Type IV by the IUPAC classification indicating that the Co@CN/GC is the mesoporous support like the CB.[40] In Figure 1b, the CB shows lager pore volume than Co@CN/GC in pore diameter over 20 nm, while Co@CN/GC exhibits larger pore volume than CB in pore diameter between 3 and 4 nm, suitable sites for deposition of Pt nanoparticles. Like the CB, both Co@CN/GC shows that the peak pore diameter under 10 nm stays at ca. 4 nm, as shown in Figure 1b inlet.

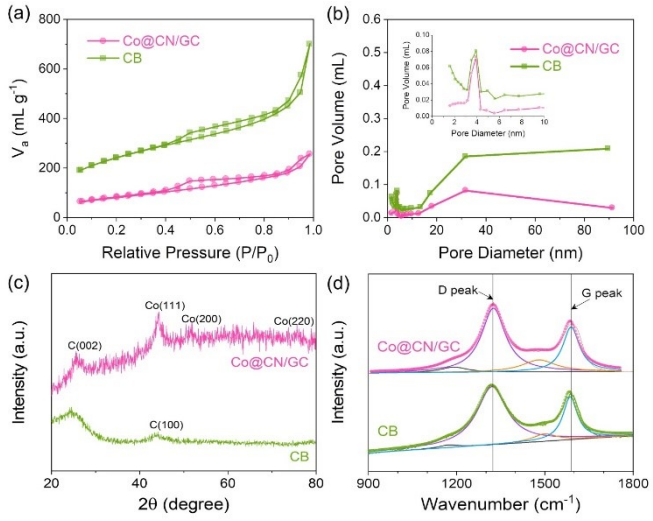

Figure 2. (a) N_2 adsorption/desorption isotherms and (b) BJH pore size distribution curves obtained from the adsorption branch of of Co@CN/GC and CB. The inset in (b) compares the pore size distribution in the range 0-10 nm. (c) XRD patterns of Co@CN/GC and CB. (d) Deconvoluted Raman spectra of Co@CN/GC and CB.

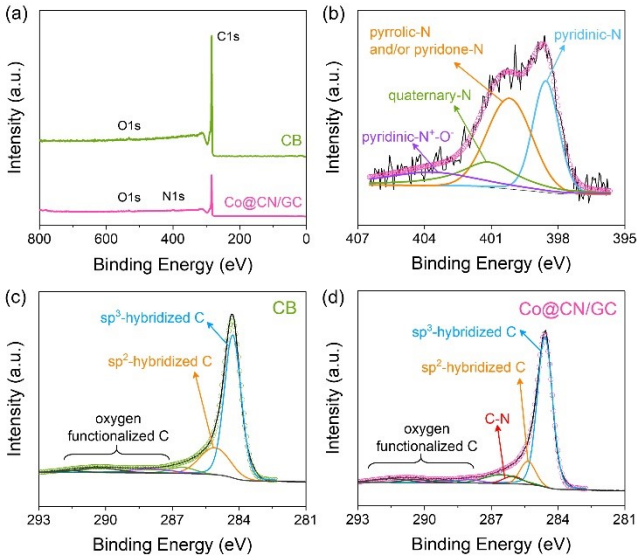

Figure 3. (a) XPS survey scans of Co@CN/GC and CB, (b) deconvoluted N 1s XPS spectra of Co@CN/GC, (c) deconvoluted C 1s XPS spectra of CB and (d) deconvoluted C 1s XPS spectra of Co@CN/GC.

To identify and compare the phase identification of a crystalline material and degree of graphitization with the CB, X-ray diffraction (XRD) patterns of the CB and Co@CN/GC are shown in Figure 1c. The Co metal is not observed in the XRD pattern of CB. The characteristic diffraction peaks of Co metal at ca. 44.2, 51.5, and 75.8° represent (111), (200), and (220) planes in Co@CN/GC support, respectively (PDF#97-007-6632). The XRD results confirm the presence of Co metal after acid-leaching at high temperature. Based on the carbon, the characteristic diffraction peaks of Co@CN/GC are sharper with increased intensity and shift to more positive angles. Therefore, the interlayer spacing of CB based on (002) plane is 0.3615 nm, while that of Co@CN/GC is 0.3463 nm. Figure 1d exhibits the Raman spectra for CB and Co@CN/GC for the sake of further confirmation on the degree of graphitization. Both CB and Co@CN/GC show the D band and G band at ca. 1350 and 1600 cm^{-1}, respectively. The D band originates from structural defects and disorder-induced features on carbon, while the G band corresponds to the stretching vibration mode of graphite crystals.[41, 42] Two broad peaks at ca. 1200 and 1510 cm^{-1} are associated with carbon atoms outside of a perfectly planar graphene network (such as aliphatic or amorphous structures) and integrated five-member rings or heteroatoms in graphene-sheet structures, respectively.[43, 44] The integrated intensity ratio of D band to the G band (I_D/I_G) is widely used for indicating the degree of graphitization or the defect quantity in graphitic materials. I_D/I_G for CB and Co@CN/GC is estimated to be 2.75 and 2.06, respectively. These results combined with the Raman spectroscopy verify that the carbon surface of Co@CN/GC has been more graphitized than CB.

XPS technique is significantly useful for the surface analysis since it measures the elemental composition, functional group, and electronic state of the elements within the Co@CN/GC. The results of XPS analysis performed on the CB and Co@CN/GC are presented in Figure 3. Figure 3a shows the

survey scans for the CB and Co@CN/GC. The nitrogen atom is not observed in the survey scan of CB. XPS spectra of Co@CN/GC show a peak at ~398 eV which corresponds to the nitrogen atom on the surface of Co@CN/GC. N 1s peak of Co@CN/GC can be deconvoluted into four major peaks corresponding to pyridinic, pyrrolic and/or pyridone, quaternary, and pyridinic-N^+-O^- (oxidized nitrogen) as shown in Figure 3b and Table S1. The peak at ca. 398.5 eV accounts for the presence of pyridinic-N whereas the peak at ca. 400.2 eV corresponds to the pyrrolic-N and/or pyridine-N. The peaks at ca. 401.1 and ca. 403.7 eV are ascribed to the presence of quaternary-N and pyridinic-N^+-O^-, respectively. For the Co@CN/GC, pyridinic-N and pyrrolic-N and/or pyridine-N contain 27.8 and 37.0%, respectively. Quaternary-N and pyridinic-N^+-O^- comprise 19.3 and 15.9%, respectively. It is well-known that quaternary-N plays an important role in the stability of catalyst in ORR, while pyridinic-N situated on the edge of the graphite planes promotes ORR by donating one p-electron to the aromatic π system.[39, 45] The incorporation of nitrogen on support can play an important role in providing active sites for the uniform Pt particle deposition and the active sites from Pt with additional activity for ORR [46, 47]. The carbon peaks for the CB and Co@CN/GC can be deconvoluted into several peaks (Table S2). For the CB in Figure 3c, C 1s peak can be divided into 6 sub-spectra, i.e., 4 oxygen functionalized carbon atoms (C-O at ca. 286.4 eV, C=O at ca. 287.9 eV, O-C=O at ca. 289.0 eV, and O-C(=O)-O at ca. 290.3 eV) and two carbon atoms in different hybridized states (sp^2 at ca. 284.3 eV and sp^3 at ca. 285.2 eV). The sp^3-hybridized carbon atoms which indicate the presence of graphite defects in the graphitic structure are present 10% in Co@CN/GC, while those in CB exhibit 20%. It is due to the decrease in graphite defects during a high-temperature treatment. The nitrogen functionalized carbon atoms (4%) in Co@CN/GC (Figure 3d) are observed at ca. 286 eV, which is in good agreement with Figure 3b.

The elemental compositions in the bulk of PtCo/NGC catalysts were determined using ICP-AES and X-ray fluorescence (XRF). For Co@CN/GC, the Co content is ca. 13 wt%. After Pt deposition, the initial Pt:Co atomic ratios are 0.9:1 for Pt/Co@CN/GC catalysts, respectively. After heat-treatment at 800 ℃ for 2 h under 5% H_2, the Pt:Co atomic ratios are 1:1 for PtCo/NGC catalysts.

To confirm the structure of PtCo alloy, different duration time from 30 min to 2 h at 800 ℃ was employed under 5% H_2 atmosphere. Corresponded XRD patterns are shown in Figure 4a. The characteristic diffraction peaks of Pt/Co@CN/GC at 39.8, 46.25, and 67.7° correspond to the (111), (200), and (220) planes of pure Pt, respectively, while those at 44.2, 51.5, and 75.8° are ascribed to (111), (200), and (220) planes of pure Co, respectively. The Pt/Co@CN/GC exhibits the characteristics of the Pt with face-centered cubic (fcc) structure. The characteristic peaks of pure Co are observed in Pt/Co@CN/GC, since the Co@CN/GC contains Co protected with graphitized CN shells. After the heat-treatment, the peaks of Co and Pt are shifted to lower and higher angles, respectively and Co diffusion into the Pt lattice is observed as indicated by the shift in Pt(111) peak to higher angles. As a result, as a duration time

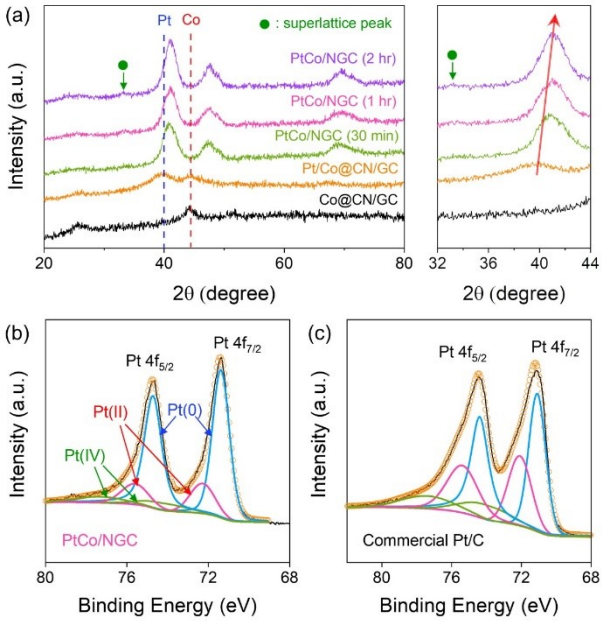

Figure 4. (a) XRD patterns of Co@CN/GC, Pt/Co@CN/GC and PtCo/NGC catalysts at 800 ℃ for different duration time (30 min, 1 h, and 2 h). Deconvoluted Pt 4f XPS spectra of (b) PtCo/NGC and (c) commercial Pt/C.

increases, the PtCo/NGC shows ordered intermetallic fct structure. The (001) and (100) superlattice planes at ca. 24 and 33°, respectively, confirm the formation of the fct phase.[48] Symmetric PtCo peaks in the catalyst heat-treated for 2 h are observed. The XRD result indicates that the Co particles embedded in the Co@CN/GC successfully diffused to the surface during heat-treatment and formed fct PtCo catalyst particles. Hereafter the PtCo/NGC catalyst heat-treated for 2 h is used for the analysis.

XPS measurements were performed to verify the oxidation states of Pt. Figure 4b and 4c show the Pt 4f spectra of Pt in PtCo/NGC and commercial Pt/C catalysts, respectively, which is deconvoluted to three pairs of doublets corresponding to metallic Pt(0), Pt(II), and Pt(IV) states. The metallic Pt(0) for PtCo/NGC is observed at 71.38 eV (Pt $4f_{7/2}$) and 74.72 eV (Pt $4f_{5/2}$), while the doublets at 72.28/75.6 and 74.2/77.32 eV could be assigned to the Pt(II) such as PtO or $Pt(OH)_2$, and Pt(IV) like PtO_2, respectively.[49, 50] The deconvoluted Pt spectra indicate that the Pt binding energy (BE) of PtCo/NGC catalyst shifts to a higher value by ca. 0.29 eV than that of commercial Pt/C catalyst. The positively shifted BE of Pt correlates to a downshift of the d-band center, which would lead to a weak chemical interaction between oxygen species and catalyst surface.[31, 51, 52] The percentage of metallic Pt(0) in PtCo/NGC catalyst, determined by the relative peak area of Pt(0) double peaks, shows 72.5%, which is even higher than that of commercial Pt/C (51.3%) due to the difference of electronegativity. It is in good agreement with literature reporting that alloying Pt with Co reduces the oxophilicity on Pt.[53, 54] The catalyst for ORR needs not to strongly bind the O or OH formed on the catalyst surface for fast H_2O desorption and high activity.[55, 56] The Co 2p XPS spectrum of PtCo/NGC shows that the dominant Co state is $Co(OH)_2$, as shown in Figure S2 and Table S3.

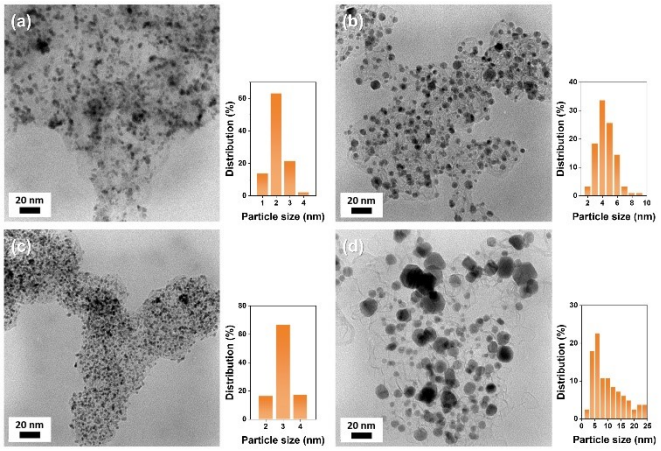

Figure 5. HR-TEM images of fresh (a) Pt/Co@CN/GC, (b) PtCo/NGC, and (c) commercial Pt/C, and (d) commercial PtCo/GC catalysts.

Catalysts	Atomic ratio (Pt:Co)	Catalyst phase	Lattice parameters a/c [nm/ nm]	Mean particle size [nm]
PtCo/NGC	1:1	ordered fct	0.2696 /0.3777	4.8
commercial PtCo/GC	2:1	disorde red fcc	0.3884 /0.3884	10.0

Table 1. Summary of structural characteristics and mean particle size of catalysts.

Figure 5a-d show the HR-TEM images of Pt/Co@CN/GC, PtCo/NGC, commercial Pt/C, and commercial PtCo/GC catalysts, respectively. Over 100 nanoparticles are used to measure the mean particle size and particle size distribution of the catalysts. As shown in Figure 5a, the Pt nanoparticles are deposited with uniform size and well-dispersed on the Co@CN/GC similarly with the commercial Pt/C. The mean particle sizes of catalysts for the Pt/Co@CN/GC and PtCo/NGC are 2.4 and 4.8 nm, respectively. For the Pt/Co@CN/GC, Pt nanoparticles in the range of 2-3 nm are dominantly deposited on Co@CN/GC. The majority of particles in PtCo/NGC are in the range of the 3-6 nm, while a few large particles are observed but well-distributed on the supports even after high-temperature treatment. However, the commercial PtCo/GC catalyst shows broad particle distribution and large mean particle size on GC. It results from that nitrogen-doped carbon surface increased the hydrophilicity of support and the charged precursor can be easily accessed on support.[57, 58] Furthermore, the efficiently controlled pyrolysis helps to alleviate the particle size growth at high temperatures.[59, 60]

It is necessary to directly observe the location of Pt and Co before and after the alloying process, which can be visible evidence for the formation of PtCo alloy. High-angle annular dark field-scanning transmission electron microscopy (HAADF-STEM) images for Pt/Co@CN/GC and PtCo/NGC catalysts are shown in Figure 6a-e. Figure 6b and S3 represent elemental mapping images for Pt/Co@CN/GC catalyst. The images clearly

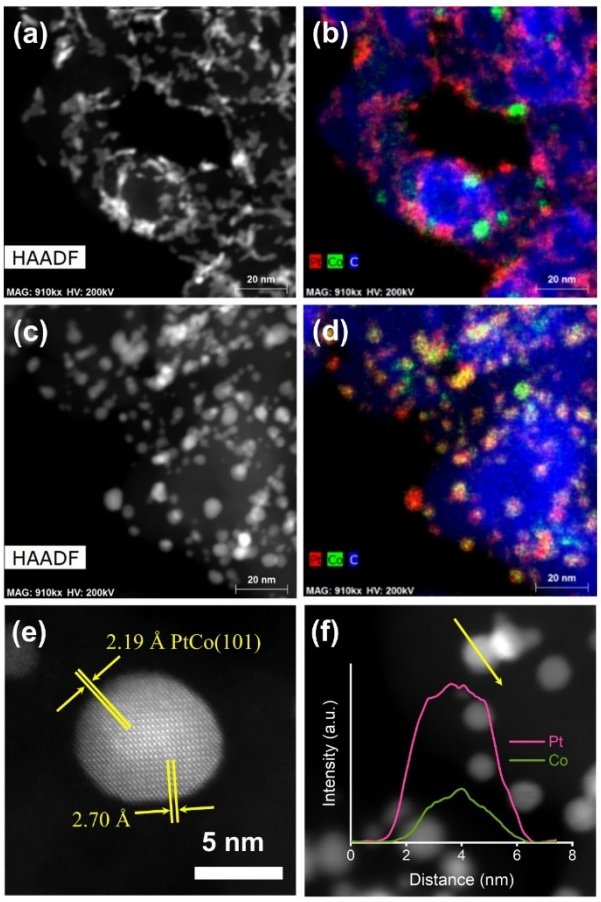

Figure 6. (a, c) HAADF-STEM images and (b, d) corresponding EDS elemental mapping images of Pt/Co@CN/GC and PtCo/NGC, respectively. (e) HAADF-STEM image of PtCo nanoparticle for PtCo/NGC. (f) XEDS line-scan of PtCo/NGC catalyst (Pt: pink and Co: green).

indicate that the Pt (red) and Co (green) particles are independently dispersed on the support. On the other hand, elemental mapping images for PtCo/NGC catalyst (Figure 6d) show that Pt and Co atoms are located at the same particles, which means that PtCo alloy is successfully formed on the low surface area support. Figure 6e exhibits that the catalyst thus prepared is the ordered intermetallic Pt alloy. Values of d-spacings calculated from Figure 6e are 2.19 and 2.70 Å which correspond to ordered intermetallic fct-structured PtCo (101) and (100) planes, respectively (PDF#97-010-2620). These results are in good agreement with XRD results. Figure 6f shows the line-scan XEDS of the PtCo/NGC catalyst. As compared to the result from the Pt/Co@CN/GC and PtCo/NGC-30min catalyst (Figure S3 and S4), Figure 6f is clear evidence for the Co diffusion into the Pt lattice during the heat-treatment process. No Co is observed for the Pt/Co@CN/GC catalyst in the line-scan XEDS result (Figure S3), while nanoparticles for the PtCo/NGC catalyst consist of Pt and Co. Furthermore, Figure 6f indicates that the catalyst particles are PtCo-core@Pt-shell structure. As indicated in Figure 6f, the Pt shell thickness observed is around 0.5-0.7 nm corresponding to 2-3 monolayers of Pt. Results from XRD and images indicate that Co encapsulated with the graphitized CN shells is slowly diffused into the Pt lattice, and then the ordered intermetallic core-shell structure catalyst is formed regardless of specific

surface area of the supports. In addition, depending on the duration time of heat-treatment, the prepared catalyst performance under MEA conditions is affected. As shown in Figure S5, The mass activity (MA), which is defined as the normalized current density measured at 0.9 $V_{iR\text{-}free}$ divided by the cathode Pt loading, increased from 0.18 to 0.45 A mg_{Pt}^{-1} as the heat-treatment time increased.

Figure 7a-c represent the polarization and power density curves of PtCo/NGC, commercial Pt/C, and commercial PtCo/GC catalysts before and after 30,000 potential cycles between 0.6 and 1.0 V, respectively, according to the AST protocol suggested by U.S. DRIVE Fuel Cell Tech Team. Initially, the PtCo/NGC, commercial Pt/C, and commercial PtCo/GC catalysts show 0.648, 0.607, and 0.566 V at 800 mA cm^{-2}, respectively. The maximum power density of PtCo/NGC catalyst is 697 mW cm^{-2}, while commercial Pt/C and commercial PtCo/GC catalysts show 651 and 482 mW cm^{-2}, respectively. It apparently indicates that the PtCo/NGC catalyst demonstrates higher performance towards ORR as a cathode catalyst than the commercial Pt/C, and commercial PtCo/GC catalysts. After AST, the potential and maximum power density of PtCo/NGC catalyst are 0.614 V at 800 mA cm^{-2} and 618 mW cm^{-2}, respectively. 34 mV loss and 11% power density loss after AST indicates that PtCo/NGC catalyst is highly stable in the conditions of practical operation. These results can also be confirmed through spectroscopic results of PtCo/NGC after AST measurement. As shown in Figure S6, the PtCo nanoparticles did not increase significantly, and the alloy was also maintained, which confirms the excellent durability of PtCo/NGC. On the other hand, potentials of the commercial Pt/C and commercial PtCo/GC catalysts exhibit negligible potentials at 800 mA cm^{-2}, while the maximum power densities of those decrease by 60 and 48% after AST, respectively. The mass activity degradation tendencies of PtCo/NGC, commercial Pt/C and commercial PtCo/GC catalysts are summarized in Figure 7d. It shows that the PtCo/NGC catalyst exhibits 0.45 A mg_{Pt}^{-1} indicating ca. 3-fold higher mass activity than that of commercial Pt/C (0.14 A mg_{Pt}^{-1}). After AST, the overall mass activity losses are ca. 53%, 70%, and 64% for PtCo/NGC, commercial Pt/C and commercial PtCo/GC catalysts, respectively. Furthermore, the PtCo/NGC still remained a remarkable amount of mass activity (0.21 A mg_{Pt}^{-1}) after AST which is even higher than that of initial mass activity of Pt/C catalyst. This may be due to the fact that the Co dissolution rate in PtCo/NGC is much smaller than that in commercial PtCo/GC and Co diffusion into the Pt lattice has increased the durability of PtCo/NGC under potential cycling conditions. The ordered intermetallic fct structure protects the transition metal composition from the corrosive environment like PEMFC operating conditions. Kim et al. reported that Fe quantity in fct PtFe was very stable for several hours, while that in fcc PtFe was dissolved within 1 h rapidly [61]. The difference in fct and fcc structure may be attributed to the favorable structure towards the ORR since there is a big difference in a lattice shape.

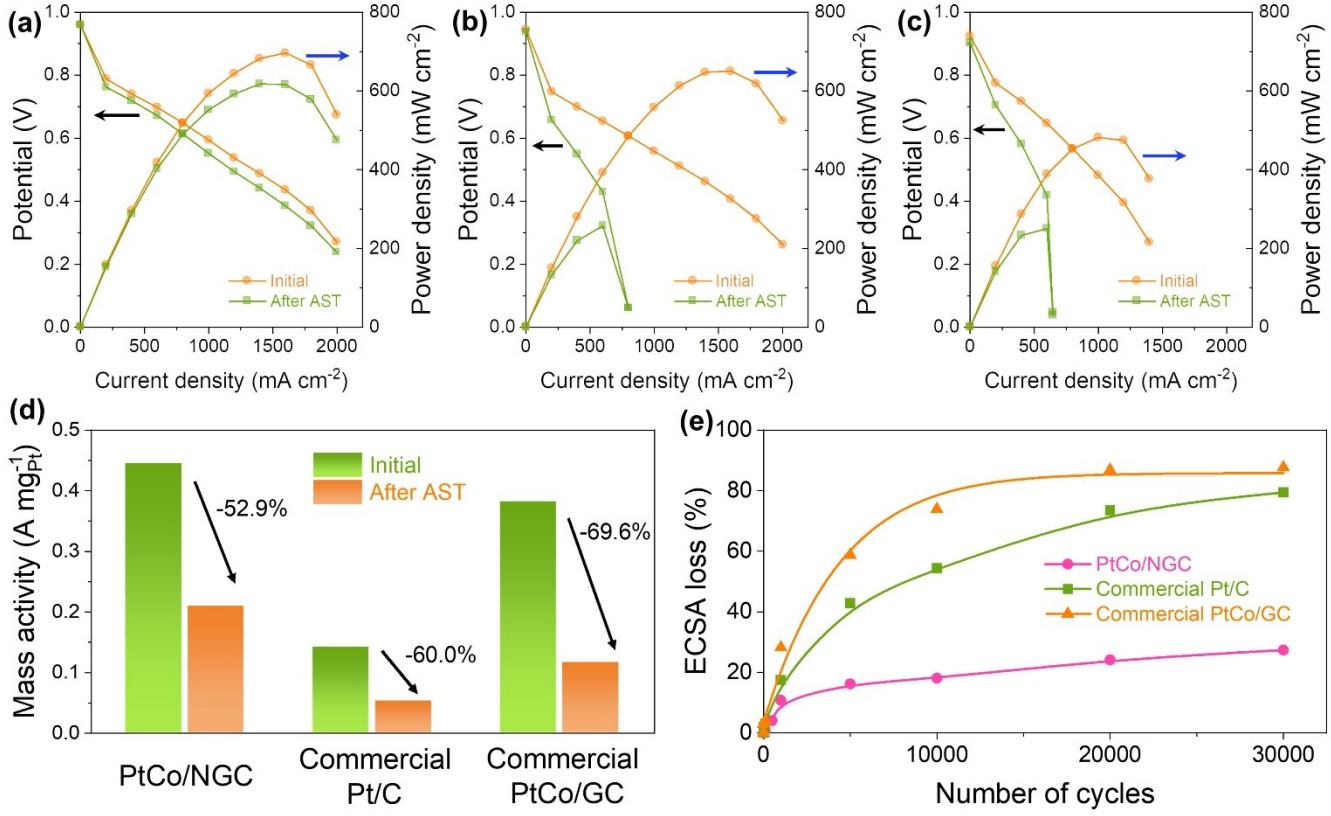

Figure 7. H_2/air polarization curves of (a) PtCo/NGC, (b) commercial Pt/C, and (c) commercial PtCo/GC catalysts before and after AST. AST was performed under 30,000 potential cycles between 0.6 and 1.0 V supplying fully humidified H_2/N_2 to anode and cathode at 80 °C, respectively. (d) Comparison of mass activities of PtCo/NGC, commercial Pt/C, and commercial PtCo/GC catalysts before and after AST. (e) Normalized ECSA loss plot of PtCo/NGC, commercial Pt/C, and commercial PtCo/GC catalysts as a function of cycle number.

Also, the large spin-orbit coupling of the Pt site and the hybridization between Fe 3d and Pt 5d states can explain the origin of fct structure on the high chemical stability.[62] To further analyze the durability of catalysts, the normalized electrochemical surface areas (ECSAs) calculated for PtCo/NGC, commercial Pt/C and commercial PtCo/GC catalysts as a function of cycle number are shown in Figure 7e. Initial ECSA values of 74, 75, and 68 $m^2\ g_{Pt}^{-1}$ are measured for PtCo/NGC, commercial Pt/C, and commercial PtCo/GC catalysts, respectively. Lower degradation rate for PtCo/NGC is observed after 5,000 cycles when compared to commercial Pt/C and commercial PtCo/GC catalysts. After 30,000 cycles, 27%, 87%, and 79% of initial ECSA are lost for PtCo/NGC, commercial Pt/C and commercial PtCo/GC catalysts, respectively, which indicate that the PtCo/NGC is remarkably stable when compared to commercial Pt/C and commercial PtCo/GC catalysts. These results indicate that the PtCo/NGC with the ordered intermetallic fct structure is remarkably durable when compared to the commercial Pt/C and commercial PtCo/GC catalyst. The intermetallic structure is known to be highly resistant to electrochemical and chemical corrosion. For example, Fe composition for disordered PtFe catalysts decreased by about 40% while the ratio of Pt to Fe in ordered intermetallic PtFe catalysts was well maintained over 6 h in strongly acidic solution.[61] As well, after 5,000 potential cycles in the half cell tests, the disordered PtCo catalyst lost more than 30 mV in its half-wave potential, while the loss of the intermetallic PtCo catalyst was only 10 mV, suggesting that the structurally ordered intermetallic catalysts were much more stable than the disordered alloy catalysts.[63] Consequently, the initial structure and compositional ratio of the intermetallic alloy catalyst could be maintained after AST. The leaching process which could form Pt oxide species was ruled out in this work to avoid the accelerated Pt dissolution. The leaching process expedited performance degradation due to Pt oxide formation, since it may be related to the Pt dissolution which possibly occurs as the Pt oxide species are reduced by the following reactions.[64]

$$PtO + 2H^+ \rightarrow Pt^{2+} + H_2O$$

$$PtO_2 + 4H^+ \rightarrow Pt^{4+} + 2H_2O$$

$$PtO_2 + 4H^+ + 2e^- \rightarrow Pt^{2+} + 2H_2O$$

On the other hand, the interactions of Pt and carbon are partially covalent and ionic since the electron delocalization between the π sites on carbon and *d* orbital of Pt, and the electron-transfer from Pt to carbon, respectively.[65, 66] Unlike the amorphous carbons, the highly graphitized carbon supports, such as CNTs and graphenes, have abundant π sites on the surface and the relatively small number of edge plane sites, which is resistant for carbon oxidation.[65, 66] Therefore, the interaction of graphitized carbon and Pt is stronger than that of amorphous carbon and Pt, which leads to less degradation. These combined effects result in high performance and stable performance after AST under PEMFC operating conditions.

4. Conclusions

A stable ordered intermetallic PtCo/NGC catalyst was successfully synthesized using thermal diffusion of Co into Pt on the N-doped GC support with a low specific surface area. The change of specific surface area, interlayer spacing, and the I_D/I_G value indicated that Co@CN/GC is more resistant for carbon oxidation when compared with the CB. HR-TEM studies indicated a presence of uniform catalyst particles with an average size of ca. 5 nm. Combined HAADF-STEM and XRD show that the ordered intermetallic fct-structured alloy possesses high stability when synthesized by thermal diffusion. XPS demonstrated that the oxophilicity of Pt has been reduced by alloying with Co which resulted O^{2-} or OH^- formed on the catalyst surface not to bind strongly, thus increasing the activity of the catalyst. The initial mass activity PtCo/NGC catalyst was estimated to be 0.45 A mg_{Pt}^{-1}. After the AST test of 30,000 potential cyles between 0.6 and 1.0 V the mass activity decreased to 0.21 A mg_{Pt}^{-1} at 0.9 $V_{iR\text{-}free}$, while the commercial Pt/C and commercial PtCo/GC catalysts showed initial mass activity of 0.38 and 0.14 A mg_{Pt}^{-1}, respectively, and 60-70% loss of the activity. PtCo/NGC catalyst exhibited higher performance than commercial catalysts and 34 mV loss and 11% power density loss after AST indicating that the PtCo/NGC catalyst was highly stable under the conditions of practical operation when compared to commercial catalysts. The enhanced catalytic performance and stability of mass activity for the PtCo/NGC catalyst are attributed to the formation of the chemically stable fct structure that alleviates the Co dissolution and controls the surface oxide thickness due to the alloy formation. In addition, the high carbon oxidation resistance of Co@CN/GC increased the durability performance at a high current density region.

Conflicts of interest

There are no conflicts to declare.

Acknowledgements

The financial support of U.S. Department of Energy (contract no. DE-EE0000460) is gratefully acknowledged. This work is also supported by the Korea Institute of Science and Technology (KIST) institutional program and the National Research Foundation of Korea(NRF) grant funded by the Korea government(MSIT) (No. 2020R1C1C1004206). We acknowledge Advanced Analysis Center at KIST for the TEM measurement.

Author Contributions

This manuscript was written through the thorough contributions of all authors.

References

1. S. R. Dhanushkodi, S. Kundu, M. W. Fowler and M. D. Pritzker, *Journal of Power Sources*, 2014, **245**, 1035-1045.
2. A. A. Topalov, S. Cherevko, A. R. Zeradjanin, J. C. Meier, I. Katsounaros and K. J. J. Mayrhofer, *Chemical Science*, 2014, **5**, 631-638.
3. X. Wang, R. Kumar and D. J. Myers, *Electrochemical and Solid-State Letters*, 2006, **9**, A225-A227.
4. F. Ettingshausen, J. Kleemann, A. Marcu, G. Toth, H. Fuess and C. Roth, *Fuel Cells*, 2011, **11**, 238-245.
5. L. Kim, C. G. Chung, Y. W. Sung and J. S. Chung, *ECS Transactions*, 2008, **16**, 945-953.
6. R. Borup, J. Davey, F. Garzon, D. Wood, P. Welch and K. More, *ECS Transactions*, 2006, **3**, 879-886.
7. S. Mitsushima, S. Kawahara, K.-i. Ota and N. Kamiya, *Journal of The Electrochemical Society*, 2007, **154**, B153-B158.
8. M. K. Carpenter, T. E. Moylan, R. S. Kukreja, M. H. Atwan and M. M. Tessema, *Journal of the American Chemical Society*, 2012, **134**, 8535-8542.
9. H. El-Deeb and M. Bron, *Electrochimica Acta*, 2015, **164**, 315-322.
10. C. Gumeci, D. U. Cearnaigh, D. J. Casadonte and C. Korzeniewski, *Journal of Materials Chemistry A*, 2013, **1**, 2322-2330.
11. X. Huang, E. Zhu, Y. Chen, Y. Li, C.-Y. Chiu, Y. Xu, Z. Lin, X. Duan and Y. Huang, *Advanced Materials*, 2013, **25**, 2974-2979.
12. V. Jalan and E. J. Taylor, *Journal of The Electrochemical Society*, 1983, **130**, 2299-2302.
13. K. Jayasayee, J. A. R. V. Veen, T. G. Manivasagam, S. Celebi, E. J. M. Hensen and F. A. de Bruijn, *Applied Catalysis B: Environmental*, 2012, **111–112**, 515-526.
14. M. K. Jeon, Y. Zhang and P. J. McGinn, *Electrochimica Acta*, 2010, **55**, 5318-5325.
15. R. Lin, T. Zhao, M. Shang, J. Wang, W. Tang, V. E. Guterman and J. Ma, *Journal of Power Sources*, 2015, **293**, 274-282.
16. S. Mukerjee and S. Srinivasan, *Journal of Electroanalytical Chemistry*, 1993, **357**, 201-224.
17. G. Sievers, S. Mueller, A. Quade, F. Steffen, S. Jakubith, A. Kruth and V. Brueser, *Journal of Power Sources*, 2014, **268**, 255-260.
18. J. Choi, J.-H. Jang, C.-W. Roh, S. Yang, J. Kim, J. Lim, S. J. Yoo and H. Lee, *Applied Catalysis B: Environmental*, 2018, **225**, 530-537.
19. J.-E. Lim, U. J. Lee, S. H. Ahn, E. Cho, H.-J. Kim, J. H. Jang, H. Son and S.-K. Kim, *Applied Catalysis B: Environmental*, 2015, **165**, 495-502.
20. B.-A. Lu, T. Sheng, N. Tian, Z.-C. Zhang, C. Xiao, Z.-M. Cao, H.-B. Ma, Z.-Y. Zhou and S.-G. Sun, *Nano Energy*, 2017, **33**, 65-71.
21. X. Peng, S. Zhao, T. J. Omasta, J. M. Roller and W. E. Mustain, *Applied Catalysis B: Environmental*, 2017, **203**, 927-935.
22. R. Wu, Y. Li, W. Gong and P. K. Shen, *ACS Sustainable Chemistry & Engineering*, 2019, **7**, 8419-8428.
23. A. S. Aricò, A. K. Shukla, H. Kim, S. Park, M. Min and V. Antonucci, *Applied Surface Science*, 2001, **172**, 33-40.
24. A. K. Shukla, M. Neergat, P. Bera, V. Jayaram and M. S. Hegde, *Journal of Electroanalytical Chemistry*, 2001, **504**, 111-119.
25. M.-k. Min, J. Cho, K. Cho and H. Kim, *Electrochimica Acta*, 2000, **45**, 4211-4217.
26. V. Stamenković, T. J. Schmidt, P. N. Ross and N. M. Marković, *The Journal of Physical Chemistry B*, 2002, **106**, 11970-11979.
27. T. Toda, H. Igarashi, H. Uchida and M. Watanabe, *Journal of The Electrochemical Society*, 1999, **146**, 3750-3756.
28. T. Toda, H. Igarashi and M. Watanabe, *Journal of The Electrochemical Society*, 1998, **145**, 4185-4188.
29. V. Stamenkovic, B. S. Mun, K. J. J. Mayrhofer, P. N. Ross, N. M. Markovic, J. Rossmeisl, J. Greeley and J. K. Nørskov, *Angewandte Chemie International Edition*, 2006, **45**, 2897-2901.
30. V. R. Stamenkovic, B. Fowler, B. S. Mun, G. Wang, P. N. Ross, C. A. Lucas and N. M. Marković, *Science*, 2007, **315**, 493-497.
31. V. R. Stamenkovic, B. S. Mun, M. Arenz, K. J. J. Mayrhofer, C. A. Lucas, G. Wang, P. N. Ross and N. M. Markovic, *Nature Materials*, 2007, **6**, 241-247.
32. D. Wang, H. L. Xin, R. Hovden, H. Wang, Y. Yu, D. A. Muller, F. J. DiSalvo and H. D. Abruña, *Nat Mater*, 2013, **12**, 81-87.
33. A. Stassi, I. Gatto, G. Monforte, V. Baglio, E. Passalacqua, V. Antonucci and A. S. Aricò, *Journal of Power Sources*, 2012, **208**, 35-45.
34. Z. Yu, J. Zhang, Z. Liu, J. M. Ziegelbauer, H. Xin, I. Dutta, D. A. Muller and F. T. Wagner, *The Journal of Physical Chemistry C*, 2012, **116**, 19877-19885.
35. B. Han, C. E. Carlton, A. Kongkanand, R. S. Kukreja, B. R. Theobald, L. Gan, R. O'Malley, P. Strasser, F. T. Wagner and Y. Shao-Horn, *Energy & Environmental Science*, 2015, **8**, 258-266.
36. J. G. McAlpin, Y. Surendranath, M. Dincă, T. A. Stich, S. A. Stoian, W. H. Casey, D. G. Nocera and R. D. Britt, *Journal of the American Chemical Society*, 2010, **132**, 6882-6883.
37. J. Stejskal and R. G. Gilbert, *Pure and Applied Chemistry*, 2002, **74**, 857-867.
38. S. Maldonado and K. J. Stevenson, *The Journal of Physical Chemistry B*, 2005, **109**, 4707-4716.
39. P. H. Matter, L. Zhang and U. S. Ozkan, *Journal of Catalysis*, 2006, **239**, 83-96.
40. K. S. W. Sing, D. H. Everett, R. A. W. Haul, L. Moscou, R. A. Pierotti, J. Rouquerol and T. Siemieniewska, *Pure and Applied Chemistry*, 1985, **57**, 603-619.
41. C. Kim, S.-H. Park, J.-I. Cho, D.-Y. Lee, T.-J. Park, W.-J. Lee and K.-S. Yang, *Journal of Raman Spectroscopy*, 2004, **35**, 928-933.
42. J. Tang, J. Yang and X. Zhou, *RSC Advances*, 2013, **3**, 16936-16939.
43. I. Herrmann, U. I. Kramm, J. Radnik, S. Fiechter and P. Bogdanoff, *Journal of The Electrochemical Society*, 2009, **156**, B1283-B1292.
44. G. Wu, C. M. Johnston, N. H. Mack, K. Artyushkova, M. Ferrandon, M. Nelson, J. S. Lezama-Pacheco, S. D. Conradson, K. L. More, D. J. Myers and P. Zelenay, *Journal of Materials Chemistry*, 2011, **21**, 11392-11405.
45. Y. Shao, J. Sui, G. Yin and Y. Gao, *Applied Catalysis B: Environmental*, 2008, **79**, 89-99.
46. D. C. Higgins, D. Meza and Z. Chen, *The Journal of Physical Chemistry C*, 2010, **114**, 21982-21988.
47. Y. Zhou, R. Pasquarelli, T. Holme, J. Berry, D. Ginley and R. O'Hayre, *Journal of Materials Chemistry*, 2009, **19**, 7830-7838.

48. S. Koh, J. Leisch, M. F. Toney and P. Strasser, *The Journal of Physical Chemistry C*, 2007, **111**, 3744-3752.
49. Y. Liang, H. Zhang, H. Zhong, X. Zhu, Z. Tian, D. Xu and B. Yi, *Journal of Catalysis*, 2006, **238**, 468-476.
50. F. Su, Z. Tian, C. K. Poh, Z. Wang, S. H. Lim, Z. Liu and J. Lin, *Chemistry of Materials*, 2010, **22**, 832-839.
51. D. S. Choi, A. W. Robertson, J. H. Warner, S. O. Kim and H. Kim, *Advanced Materials*, 2016, **28**, 7115-7122.
52. B. Y. Xia, H. B. Wu, N. Li, Y. Yan, X. W. Lou and X. Wang, *Angewandte Chemie International Edition*, 2015, **54**, 3797-3801.
53. J. Xu, X. Liu, Y. Chen, Y. Zhou, T. Lu and Y. Tang, *Journal of Materials Chemistry*, 2012, **22**, 23659-23667.
54. J. Zeng and J. Y. Lee, *Journal of Power Sources*, 2005, **140**, 268-273.
55. GreeleyJ, I. E. L. Stephens, A. S. Bondarenko, T. P. Johansson, H. A. Hansen, T. F. Jaramillo, RossmeislJ, ChorkendorffI and J. K. Nørskov, *Nat Chem*, 2009, **1**, 552-556.
56. Y. Kim, Y. Kwon, J. W. Hong, B.-S. Choi, Y. Park, M. Kim and S. W. Han, *CrystEngComm*, 2016, **18**, 2356-2362.
57. G. Bae, D. H. Youn, S. Han and J. S. Lee, *Carbon*, 2013, **51**, 274-281.
58. Y. Chen, J. Wang, H. Liu, M. N. Banis, R. Li, X. Sun, T.-K. Sham, S. Ye and S. Knights, *The Journal of Physical Chemistry C*, 2011, **115**, 3769-3776.
59. W. Jung, T. Xie, T. Kim, P. Ganesan and B. N. Popov, *Electrochimica Acta*, 2015, **167**, 1-12.
60. T. Xie, W. Jung, T. Kim, P. Ganesan and B. N. Popov, *Journal of The Electrochemical Society*, 2014, **161**, F1489-F1501.
61. J. Kim, Y. Lee and S. Sun, *Journal of the American Chemical Society*, 2010, **132**, 4996-4997.
62. T. Burkert, O. Eriksson, S. I. Simak, A. V. Ruban, B. Sanyal, L. Nordström and J. M. Wills, *Physical Review B*, 2005, **71**, 134411.
63. D. Wang, H. L. Xin, R. Hovden, H. Wang, Y. Yu, D. A. Muller, F. J. DiSalvo and H. D. Abruña, *Nature Materials*, 2013, **12**, 81-87.
64. W. S. Jung and B. N. Popov, *ACS Sustainable Chemistry & Engineering*, 2017, **5**, 9809-9817.
65. X. Yu and S. Ye, *Journal of Power Sources*, 2007, **172**, 145-154.
66. F. Coloma, A. Sepulvedaescribano and F. Rodriguezreinoso, *Journal of Catalysis*, 1995, **154**, 299-305.

Graphical Abstract

Title
Highly Stable Ordered Intermetallic PtCo Alloy Catalyst Supported on Graphitized Carbon Containing Co@CN for Oxygen Reduction Reaction

Authors
Won Suk Jung, Woong Hee Lee, Hyung-Suk Oh, and Branko N. Popov

Keywords
Proton exchange membrane fuel cells; Oxygen reduction reaction; Intermetallic alloy; Potential cycling; Stability

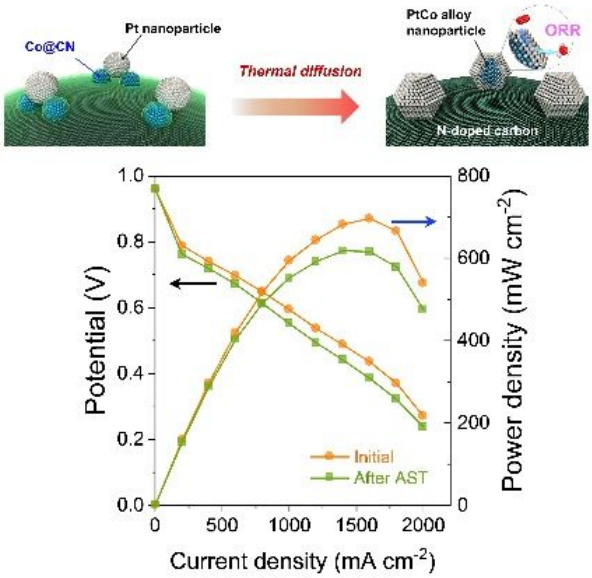

Ordered intermetallic PtCo synthesized from N-doped graphitic carbon-containing Co presents the high durability with low Pt loading after 30,000 load-simulated cycles in proton exchange membrane fuel cells. This makes a significant contribution to the literature because the durability issue for the ORR electrocatalysts under the real operating condition is important for the fuel cell vehicle.